

High-quality and field resilient microwave resonators on Ge/SiGe quantum well heterostructures

Luigi Ruggiero¹, Carlo Ciaccia¹, Pauline Drexler², Vera Jo Weibel¹, Christian Olsen¹, Christian Schönenberger^{3, 4}, Dominique Bougeard², and Andrea Hofmann^{1, 3, 5}

¹ University of Basel, Klingelbergstrasse 82, 4056 Basel, Switzerland

² Fakultät für Physik, Universität Regensburg, Universitätsstraße 31, 93053 Regensburg, Deutschland

³ Swiss Nanoscience Institute, Klingelbergstrasse 82, 4056 Basel, Switzerland

⁴ YQuantum, Parkstrasse 1, 5234 Villigen, Switzerland

⁵ Corresponding author, email: andrea.hofmann@unibas.ch

December 24, 2025

Superconducting resonators integrated with **germanium (Ge) quantum wells (QWs)** offer a promising platform for hybrid quantum devices. Yet, in the most common heterostructure architectures, they have so far been limited by sizable photon losses. Here, we report the fabrication and characterization of microwave resonators patterned in the **aluminum (Al)** thin film of an in-situ grown superconductor/semiconductor hybrid **heterostructure (HS)**. The semiconductor part of this hybrid **HS** is grown on a commercial **Ge** substrate. We consistently achieve internal quality factors $Q_i > 1000$, surpassing previous results on **Ge QW** heterostructures grown using the concept of a virtual **Ge** substrate on **silicon (Si)** substrates. We reach $Q_i \approx 49000$ at single-photon occupation and a plateau of $Q_i \approx 20000$ at sub-one photon, an order of magnitude larger than any previously reported value of resonators on **Ge QW** structures at low power. We further characterize the thin **Al** film forming the resonator, extracting its kinetic inductance and superconducting gap, and studying its magnetic field dependence. Notably, the resonance remains well-defined up to in-plane magnetic fields of 850 mT. With a hysteresis emerging in the out-of-plane magnetic field dependence, for both the resonance frequency and the quality factor, indicating an interesting interplay between vortex- and quasiparticle loss mechanisms.

I. INTRODUCTION

Strained **Ge QWs** are a promising platform for both spin qubits [1–3] and hybrid quantum devices [4–6]. Integration of these devices with microwave resonators [7–11] is attractive as it enables fast, high-fidelity readout and offers a route toward long-range qubit coupling via cavity photons [12–14]. However, combining a compact heterostructure architecture with high-quality resonators has been challenging so far, mainly due to the lossy substrate originating from specific growth techniques. The strained **Ge QW** is built by growing a thin layer of **Ge** in-between two strain-relaxed **Ge-rich SiGe** layers. Starting from a commercial **Si** substrate, the unstrained **SiGe** layer is obtained via a strain-relaxing buffer [15], either by gradually increasing the **Ge** content, or by first growing a pure **Ge** layer and subsequent decreasing of the **Ge** content. This latter approach has recently gained increased attention due to the reported high mobilities and successful qubit operations performed on such heterostructures [2, 16]. However, it contains many dislocations at the **Si-Ge** interface, due to the large lattice mismatch of the two materials. The microwave losses introduced by these defects limit the reported Q_i to about 1000 [11]. On the other hand, larger Q_i values of a few thousand have been achieved [7–10] by the former approach, at the cost of thick buffer layers and long growth times. Additionally, most studies on microwave resonators on **Ge** have so far been limited to low fields, even though analyses on field

resilience [8] are crucial for qubit applications.

Here, we present an approach delivering high Q_i and a large in-plane magnetic field resilience for resonators which are structured into a **molecular-beam epitaxy (MBE)** grown superconductor/semiconductor hybrid **HS**. Different from many existing **Ge/silicon-germanium (SiGe) HSs** [1–11], our hybrid **HS** is grown on a commercial **Ge** substrate with appropriate grading to a constant **SiGe** composition [17]. This allows us to avoid the dislocation density-rich **Si-Ge** interface, which provides loss-channels for the resonator [7], and still keep the **HS** stack compact. The hybrid **HS** is furthermore characterized by an in-situ grown thin superconducting **Al** film, brought onto the semiconductor without breaking the vacuum. To characterize the material platform and its suitability for microwave technology, we systematically compare eight resonators of varying lengths and investigate the dependence of Q_i and resonance frequency on applied magnetic fields.

II. EXPERIMENTAL

A. Hybrid heterostructure and setup

The **MBE**-grown hybrid superconductor/semiconductor **HS** used here features an 8 nm thin **Al** film directly grown onto a **Ge/SiGe HS** with a **Ge QW**. The whole stack, including the 475 μm thick

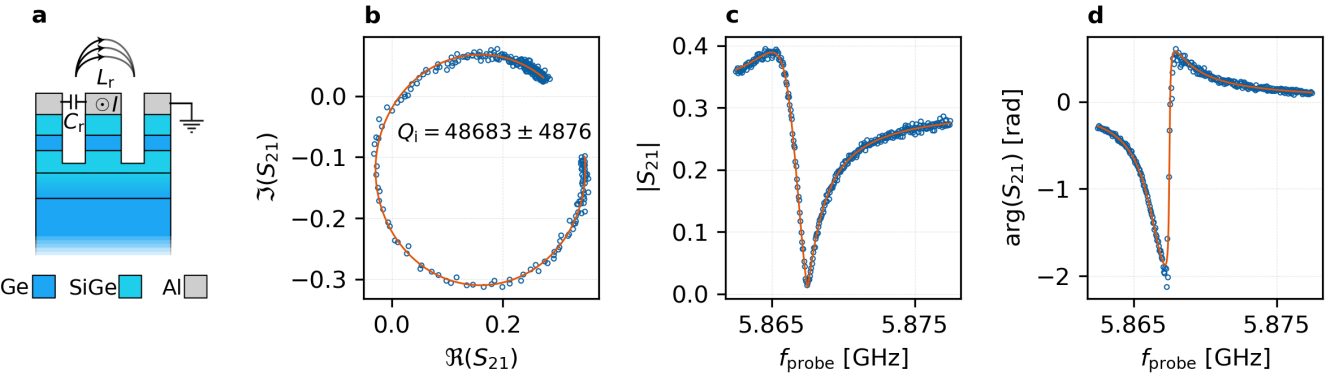


FIG. 1: **High-Q resonator on a Ge QW.** (a) Cross-sectional schematic (not to scale) of a microwave resonator patterned from an Al film deposited on a Ge/SiGe quantum well, which is epitaxially grown on a Ge substrate. (b - d) Fit (orange solid line) of the I/Q, transmission amplitude and phase response, respectively. The extracted quality factor exceeds 4.8×10^4 at an average circulating photon number of $\langle n_p \rangle \approx 1.0$.

commercial Ge substrate, is shown in Figure 1(a). Detailed information on the growth can be found in the Supplementary Information. The transmission line (TL) and the resonators are carved out of the Al film by standard Transene-D wet-etching of the Al followed by reactive ion etching (RIE) of the HS. The Ge/SiGe QW remains intact below the resonator.

We measure three samples: Sample A with eight $\lambda/4$ resonators hanging to a TL, and samples B and C with a single $\lambda/4$ resonators hanging to a TL. In all the samples, the TL is much longer than the resonators and designed to be 50Ω -matched at both ends (see Supplementary Information) in order to avoid interference of standing waves. The experiment is designed such that we can separately estimate the internal quality factor Q_i and the coupling quality factor Q_c , from which we extract the loaded quality from $1/Q_1 = 1/Q_i + 1/Q_c$. Unless specified otherwise, the experiments are carried out in a dilution refrigerator (DR) with a base temperature of 10 mK , using a Rohde&Schwarz ZNB8 vector network analyzer. The input line is attenuated inside the DR allowing for low powers down to below one average circulating photon in the resonator. We measure the transmitted signal through the TL S_{21} , which travels through a superconducting coaxial cable up to 4 K , where it is amplified by a Low Noise Factory LNF_LNC1_12A High Electron Mobility Transistor (HEMT) amplifier, the signal is amplified again at room temperature with an additional amplifier Miteq AMF-3F-01000400-08-10P.

In a first set of experiments, sample A is cooled down in the DR with a passive Al magnetic field shield. The ground plane is connected through several Al bonds to the ground of the cryostat. Additional bonds bridging across each resonator and the TL aim to further reduce potential inhomogeneities of the ground plane. The Printed Circuit Board (PCB) is embedded in a copper (Cu) box in order to minimize the impact of standing waves.

With this setup, we achieve an internal quality factor $Q_i = (48683 \pm 4876)$ at low input power P_{in} corresponding to an average number $\langle n_p \rangle = (2P_{\text{in}}Q_i^2)(\hbar\pi f_r Q_c) \approx 1$ photon circulating in the resonator [18]. The internal Q_i and external quality factor Q_c , as well as the resonator resonance frequency, are extracted from a circular fit [19] of the resonator response in the complex plane, as shown in Figure 1(b - d). The resonance frequency, f_r , has been determined by measuring the complex transmission as a function of frequency, where the absolute value shows a dip and the phase response shows a characteristic jump at resonance, see Figure 1(b) and (c), respectively. The extracted f_r amounts to 5.86 GHz and the coupling quality factor is $Q_c = (2531 \pm 21)$. Although here, the coupling quality factor limits the photon lifetime, the design can easily be adjusted to a higher Q_c . Meanwhile, the extracted Q_i corresponds to a photon lifetime of $Q_i/(2\pi f_r) \approx 2.6 \text{ } \mu\text{s}$, which exceeds the coherence times of many reported qubits in Ge [1, 2, 20].

B. Film characterization

In contrast to other experiments performed on Ge/SiGe HSs where ex-situ deposited Al layers are used to induce a proximity effect [21], our resonators are directly fabricated from a hybrid HS (see Supplementary Information). The MBE-approach provides a high degree of control of the Al film thickness and allows to form an abrupt superconductor/semiconductor interface (see transmission electron microscopy (TEM) in Supplementary Information), via crystalline growth in an ultra-high vacuum (UHV) environment.

We first characterize the kinetic inductance L_{kin} of the Al film. To do so, we measure the dependence of the resonance frequency on the resonator's length l , as shown in Figure 2(a). We fit our data to $f_r(l) = 1/4l\sqrt{L_r C_r}$ valid for the employed quarter-wavelength geometry. Here,

$L_r = L_{\text{geo}} + L_{\text{kin}}$, $L_{\text{geo}} = (\mu_0/4)(K(k'_0)/K(k_0)) = 26.6 \text{ nH/m}$ is the geometric inductance per unit length, $C_r = 4\epsilon_0\epsilon_{\text{eff}}K(k'_0)/K(k_0)$ is the capacitance per unit length [22], and ϵ_{eff} the material's dielectric constant. Using the dielectric constant and kinetic inductance as fitting parameters, we extract $\epsilon_{\text{eff}} = (10.01 \pm 0.01)$ and $L_{\text{kin}} = (36 \pm 2) \text{ pH}/\square$. With our 8 nm Al film, we find that the kinetic inductance is four times larger than reported for a 10 nm thick Al film grown ex-situ onto a QW HS in ultra-high vacuum environment [21], consistent with the fact that L_{kin} increases for thinner superconducting films.

To further characterize the Al film in terms of its superconducting properties, we analyze the resonance frequency as a function of temperature. It follows a Bardeen–Cooper–Schrieffer (BCS)-like behavior, where the Cooper pair density decreases at elevated temperature, increasing the kinetic inductance and reducing the resonance frequency. We fit $(f_r - f_{r,10 \text{ mK}})/f_{r,10 \text{ mK}} = -\alpha/2\sqrt{\pi\Delta_0/(2k_B T)} \exp(-\Delta_0/(k_B T))$ to the data shown in Figure 2(b) [23, 24], where $f_{r,10 \text{ mK}}$ refers to the resonance frequency at 10 mK and $\alpha = L_{\text{kin},0}/(L_{\text{kin},0} + L_{\text{geo}})$ is the kinetic inductance fraction at zero temperature. We extract a superconducting gap at zero temperature $\Delta_0 = (298 \pm 4) \mu\text{eV}$, slightly higher than in a 10 nm thick Al film grown ex-situ onto a QW HS in UHV environment [21]. Further, we extract the kinetic inductance fraction $\alpha = (0.75 \pm 0.08)$ from the fit, in agreement with the value obtained from calculating $\alpha_{\text{sim}} = 0.85$ from the inductance values L_{kin} and L_{geo} .

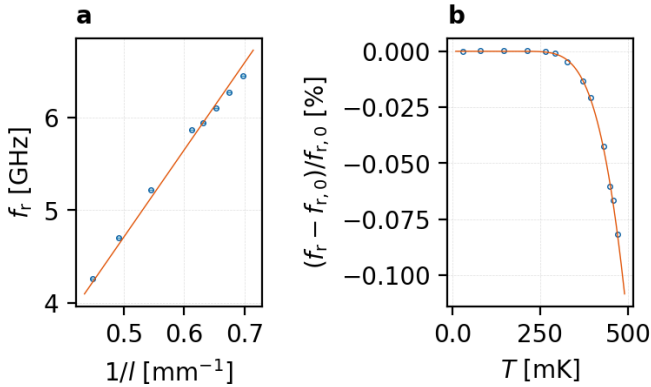


FIG. 2: Thin film properties extracted from resonator characteristics. (a) The resonance frequency f_r is inversely proportional to the resonator length l . The data (blue dots) are fitted (solid line) to the equation $f_r(l)$ specified in the main text, yielding a kinetic inductance of $(36 \pm 2) \text{ pH}/\square$ (b) The relative shift of the resonance frequency f_r (blue dots) measured at elevated temperature compared to $f_{r,0} := f_{r,T=10 \text{ mK}}$. The solid line is a fit to the BCS theory (see main text), which predicts a decreasing resonance frequency due to the lower density of Cooper pairs which increases the kinetic inductance.

C. Statistics on Q_i

To gain insight into the variability of our resonators, we analyze and compare the performance of eight different resonators all patterned on the same sample A. In Figure 3(a) we plot Q_i for all eight resonators as a function of average photon number. A sketch of the design and an optical image of the bonded device are shown in Figure 3 (b) and (c), respectively. The inset of Figure 3(c) highlights the position of the best resonator relative to the whole sample described in section II B, showing all relevant dimensions. The chosen design yields impedance values slightly above 50Ω , and we consistently measure quality factors exceeding 1000. Thus, higher than what previously reported for resonators on Ge/SiGe HSs grown via Ge virtual substrates on commercial Si substrates [11] and similar to those on HSs grown directly on commercial Si [9, 21]. This corroborates previous suspicions [11] that the defects at the interface between the Si substrate and the Ge virtual substrate are the main source of loss.

The origin of the losses can be better understood by sweeping the input power circulating in the resonator. The Q_i of some of the resonators exhibits an increase with power before saturating at higher levels. This behavior is characteristic of resonator loss dominated by two-level systems (TLS), which cause dissipation at low photon numbers [25]. As the power increases, the TLS gradually saturate, reducing their contribution to loss and resulting in a plateau in Q_i at high power. The onset of this increase depends on factors such as the resonance frequency, the coupling strength to TLS, and the internal quality factor at low photon numbers. For most of our resonators, we observe this increase in Q_i already at relatively low powers. Notably, in the resonator with the highest observed Q_i , we also detect a plateau at low photon number, indicating a regime where unsaturated TLS dominate the loss [25]. In this case, Q_i plateaus at approximately 20 000 at average photon numbers well below one.

For some of the resonators, we observe no pronounced dependence of Q_i on input power, suggesting that loss mechanisms other than TLS dominate [11]. One possible source is an etching imperfection in the TL, as indicated by a dashed red rectangle in Figure 3(c), which may disrupt the homogeneity of ground currents or promote quasiparticle excitations. The relative significance of TLS loss—quantified by the difference in Q_i between low and high power or $Q_{i,\text{max}}$ —clearly correlates with the resonator's proximity to this defect (see Supplementary Information). Additionally, the placement of bond wires has been shown to influence resonator performance by altering the distribution of ground currents [26, 27]. Nevertheless, all the resonators consistently display high internal quality factors above 1000.

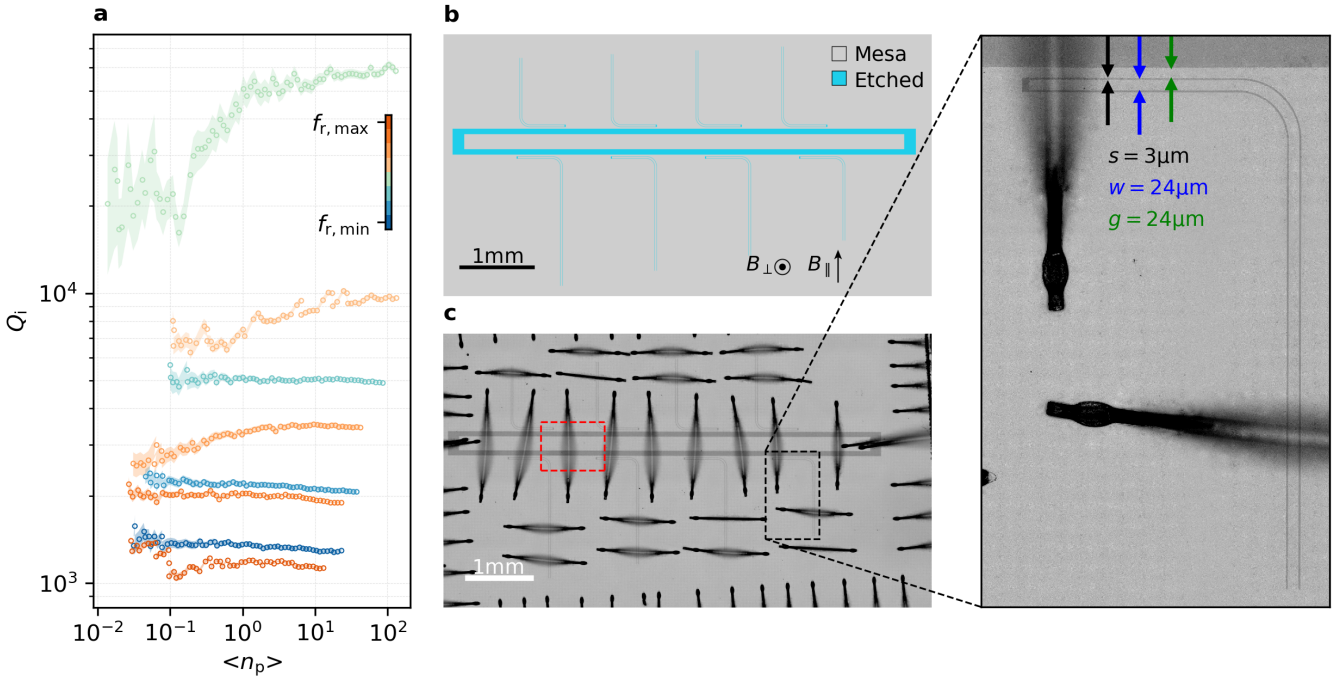


FIG. 3: **Photon number dependence of eight $\lambda/4$ resonators connected to a single TL.** (a) Quality factor as a function of average photon number for eight resonators of different frequencies ranging from about 4 GHz to 7 GHz. (b) Design scheme with eight $\lambda/4$ resonators of different length l hanging to a common TL. (c) Top view of the sample on which the design in (b) is patterned. The impedance of the resonators at resonance frequency is $Z_r = \sqrt{L_r/C_r} \approx 66 \Omega$ [22]. The constant coupling length of 473 μm (not shown) and its relative variation to resonator length yields a variable coupling quality factor Q_c ranging from 1200 to 9000 in agreement with the simulations shown in SFig.2(b). It is also affected by grounding inhomogeneities, which we try to minimize by bonds connecting different areas of the ground plane. The area marked by red dashed line indicates a region of inhomogeneous etching. (c.inset) Zoom-in on the resonator with the highest quality factor, with details on the feedline width $w = 24 \mu\text{m}$, gap to ground $s = 3 \mu\text{m}$, coupling $g = 24 \mu\text{m}$, constant for all eight resonators.

D. Impact of magnetic field

For future qubit applications, information on the response of the resonators to magnetic fields will be important. We study the in-plane characteristics using sample B, which contains a resonator with $f_r = 3.76 \text{ GHz}$ and $Q_{i,B_{\parallel}=0} = 1150$ measured at base temperature, high photon number and zero applied field. Note that vortices in the magnet coil likely decrease the quality factor from its true zero-field value. The design of the transmission line is the same as used for sample A, and the coupling length of the same order. The in-plane field, defined as shown in Figure 3 (b), is produced by a vector magnet, which allows for a correction of a small sample tilt estimated to $\theta \approx 0.12^\circ$ by adjusting different axes of the vector magnet during the sweep.

In Figure 4, we plot the shift in resonance frequency, $\delta f_r = f_r(B_{\parallel} = 0) - f_r(B_{\parallel} > 0)$ and the normalized quality factor $Q_i(B_{\parallel} > 0)/Q_i(B_{\parallel} = 0)$. The resonance frequency starts to shift significantly only at fields above 100 mT, due to lower density of Cooper pairs increasing the kinetic inductance. Regarding the quality factor, we choose to plot relative values, as the presence of vortices in the vector magnet reduces the zero-field Q_i

compared to measurements performed in a magnet-free, shielded setup. The quality factor tends to decrease with increasing field, though its behavior is heavily affected by the fluctuations of the vector magnet and the vortices trapped in the superconducting film. Nevertheless, the quality factor has decreased by less than 75 % at 850 mT. At this field, we can still perform a reliable fit to the dip in the transmission amplitude.

The resonator's behavior in out-of-plane magnetic fields is studied using sample C, which carries a resonator with $f_r = 3.45 \text{ GHz}$ and $Q_{i,B_{\perp}=0} \approx 5000$. The results are shown in Figure 4(c-d), showing a pronounced hysteresis. While the best possible quality factors are likely obtained by releasing vortices after each change of the magnetic field, such a scenario is not realistic for actual (qubit) device measurements. Hence, it is important to analyze the hysteresis, which we believe is caused by an interplay between vortex dynamics in the superconducting film and quasiparticle excitation and trapping. The out-of-plane field is supplied by a homemade superconducting coil mounted on the back of the PCB, all the components are encapsulated in an Al magnetic field shield. Starting from zero field, the resonance frequency decreases gradually with increasing field. This is partly due to a narrow-

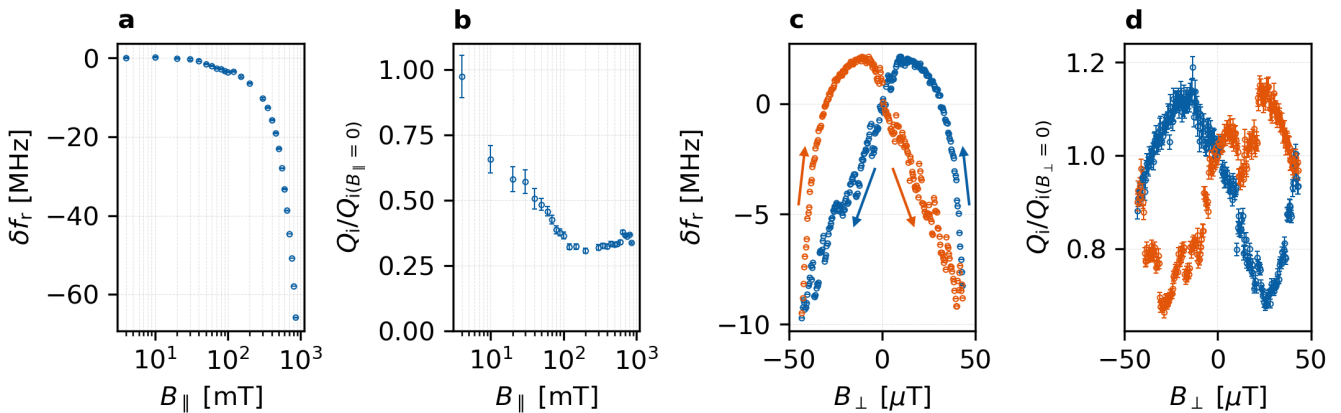


FIG. 4: **Magnetic field dependence.** (a) Shift of the resonance frequency and (b) normalized quality factor as a function of in-plane magnetic field from zero to $B_{\parallel} = 850$ mT. (c) Shift of the resonance frequency and (d) normalized quality factor as a function of out-of-plane magnetic field from zero to $B_{\perp} = 50$ μ T. The arrows and the color (orange for increasing fields and blue for decreasing fields, respectively) indicate the direction of the sweep.

ing of the effective width of the superconducting region in the center line, and partly due to a slow buildup of vortices [28, 29]. Superimposed on this trend, we observe noise attributed to flux avalanches [30], clearly discernible in Figure 4(c) as jumps in the f_r dependence as the field is swept from zero towards positive/negative values. When sweeping the field back towards zero, vortices are rapidly annihilated [28, 29] by antivortices formed due to the local internal field reversing polarity before the external field crosses zero [30]. The decreasing vortex density causes a sharp rise in resonance frequency, which reaches a maximum just before the applied field returns to zero, indicating a point of minimal vortex density.

Concurrently, the quality factor initially increases with field due to trapping of quasiparticles by vortices. However, as the vortex density grows, their dissipative effect outweighs the benefits of quasiparticle trapping, and the quality factor begins to decline. Upon sweeping the field back to zero, the quality factor drops even further, although the strong frequency increase suggests efficient vortex annihilation. We interpret this somewhat uncommon observation as an indication that vortices in our system are highly effective at suppressing quasiparticle-induced loss. Their rapid removal therefore enhances the effect of quasiparticle dissipation. The quality factor starts to rise at small fields, when the quasiparticle density decreases and their trapping becomes more efficient.

III. CONCLUSION

We demonstrate high-quality microwave resonators in a Ge-based hybrid HS. Unlike previous implementations of such resonators, our Ge/SiGe QW structure is grown on a Ge substrate, and the Al film is deposited in-situ, via MBE, as an integral part of the hybrid HS. This approach

enables to grow a compact semiconductor part of the hybrid HS without introducing a lossy Ge-on-Si interface. The in-situ MBE growth also facilitates the realization of ultra-thin Al films with a high kinetic inductance. While this is not the focus of this study, we suspect the in-situ integration of the hybrid HS to additionally provide a clean superconductor–semiconductor interface (see TEM in Supplementary Information).

We extract internal quality factors, with $Q_i \approx 49000$ in the quantum regime (single-photon), $Q_i > 20000$ in the unsaturated TLS regime, and we measure Q_i up to $Q_i \approx 60000$ at high power. These values suggest long coherence times even when integrated with a quantum device. The resonators are compatible with large in-plane magnetic fields corresponding to Zeeman energies of 10 μ eV for typical in-plane g -factors in Ge quantum dots [20, 31]. We also characterize the hysteresis in resonance frequency and quality factor under out-of-plane magnetic fields, indicating a complex interplay between quasiparticles and vortices.

IV. FUNDING STATEMENT

This work was supported as a part of NCCR SPIN, a National Centre of Competence in Research, funded by the Swiss National Science Foundation (grant number 225153), by the European Union’s Horizon 2020 research and innovation program through the Marie Skłodowska Curie COFUND project QUSTEC, agreement No 847471, by the Swiss National Science Foundation through grant 192027 and by the Basel QCQT PhD school. The research is part of the Munich Quantum Valley, which is supported by the Bavarian state government with funds from the Hightech Agenda Bavaria.

Supplementary Material

Appendix A: Superconductor/Semiconductor hybrid heterostructure epitaxy

The heterostructure is grown on a 475 μm thick commercial Ge(001) substrate using solid-source MBE. To gradually relax the strain created by lattice mismatch, a 670 nm concentration graded $\text{Si}_{1-x}\text{Ge}_x$ buffer using the concept of linear grading of x is deposited onto the substrate. The final composition is $\text{Si}_{0.2}\text{Ge}_{0.8}$. The graded buffer is followed by a $\text{Si}_{0.2}\text{Ge}_{0.8}/\text{Ge}/\text{Si}_{0.05}\text{Ge}_{0.95}$ QW, with the respective layer thicknesses 460/15/5 nm.

The superconductor/semiconductor (super/semi) hybrid heterostructure is then completed in an MBE chamber dedicated to metal and oxide growth. The transfer between the chambers is performed without breaking the ultra-high vacuum (UHV, $<10^{-10}$ mbar). To favor the growth of a continuous, crystalline 8 nm Al film, the substrate is cooled to approximately -100°C before the Al growth. To prevent uncontrolled oxidation of the Al layer in air after the epitaxy, a 2 nm aluminum oxide capping layer is deposited in situ. Subsequently, the wafer is transferred, again without breaking the UHV, into a dedicated oxidation chamber, where it is exposed to pure oxygen at $3 \cdot 10^{-6}$ mbar for 10 minutes.

Fig. 5 shows a high-angle annular dark-field (HAADF) transmission electron micrograph (TEM) of the as-grown interface between the $\text{Si}_{0.2}\text{Ge}_{0.8}/\text{Ge}/\text{Si}_{0.05}\text{Ge}_{0.95}$ semiconductor QW and the Al superconductor film.

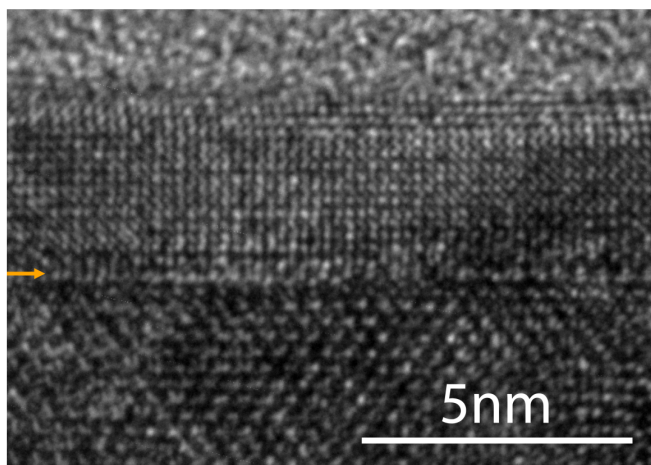


FIG. 5: **TEM characterization.** HAADF image of the super/semi interface indicated by the orange arrow, with on top the Al and on the bottom the $\text{Si}_{0.05}\text{Ge}_{0.95}$ top barrier of the QW.

Appendix B: Transmission line design

The **TL** is designed to be 50Ω -matched, however considering the relation $L_{\text{kin}} \gg L_{\text{geo}}$ valid for our superconducting film, this is not trivial and straightforward. A first resonator couple to a **TL** was designed in order to estimate L_{kin} , afterwards this value was used as input in *Sonnet* to estimate the optimal dimensions of the **TL** in order to achieve the optimal 50Ω . The value is based on what is extracted for the simulation, however, the transmission amplitude in our experiments matches well the amplification and attenuation of the lines, proving the **TL** impedance is not too far off 50Ω .

Appendix C: Inhomogeneous Etching

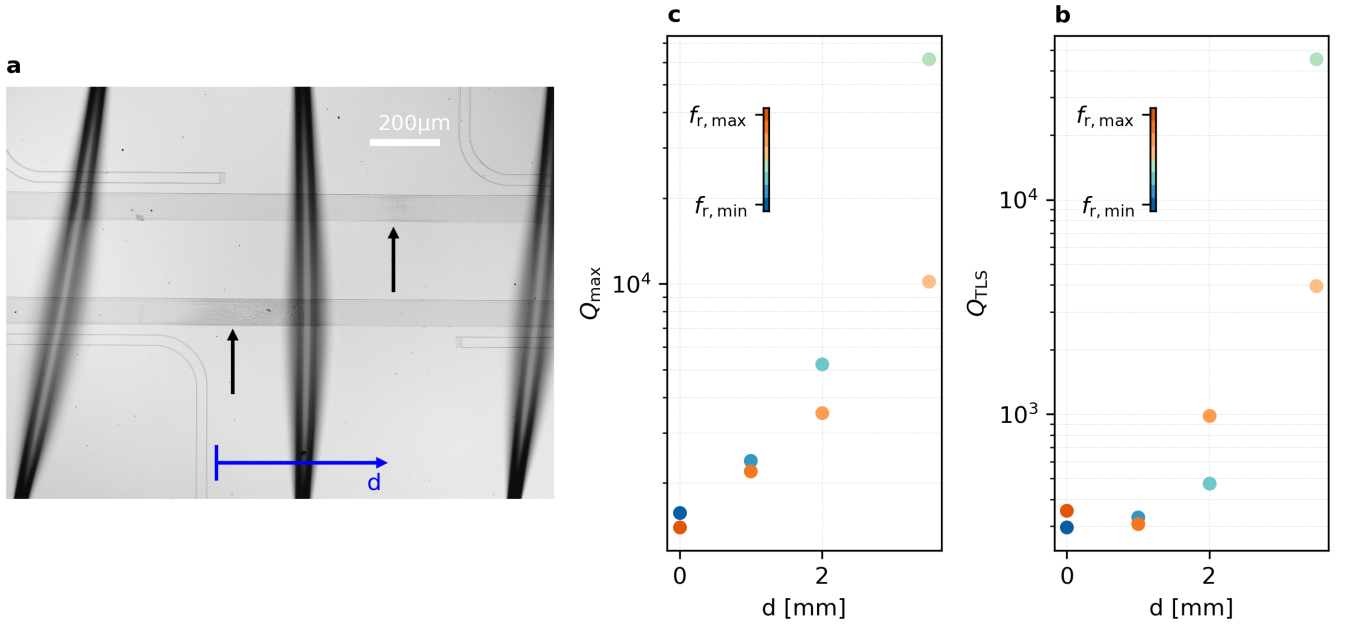


FIG. 6: **Impact of inhomogeneous etching on the Q_i .** (a) Optical image of the sample with focus on the inhomogeneous etching of the **TL** trenches indicated by the black arrows. (b) Max internal quality factor as a function of the distance d from the "dirty spot" in (a). (c) Q_{TLS} defined as the difference between the Q_i at high photon number and saturated **TLS** and the Q_i at low photon number as a function of the distance d from the "dirty spot" in (a).

Appendix D: Simulations

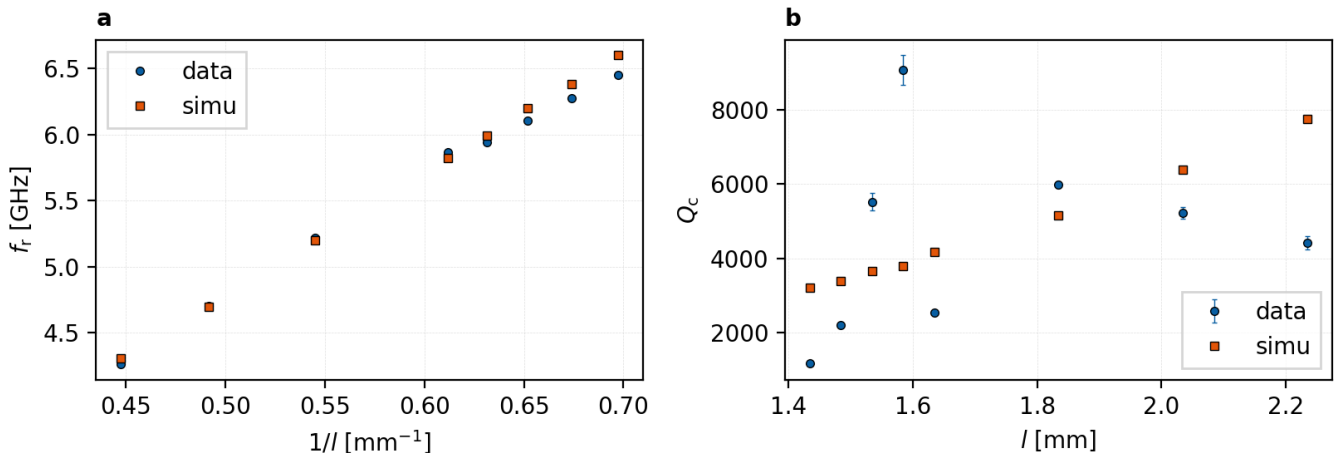


FIG. 7: **Sonnet simulations.** (a) Comparison between f_r as a function of length extracted from the data and estimated from the simulations using $L_{\text{kin}} = 36 \text{ pH}/\square$ and ϵ_{rel} of bulk Ge of 15.8 [32] as input parameters. (b) Comparison between Q_c as a function of length extracted from the data as a function of length and estimated from the simulations. Except for some fluctuations the data are in agreement with the theory. (b) Simulated characteristics impedance Z_0 as a function of frequency.

[1] N. W. Hendrickx, D. P. Franke, A. Sammak, G. Scappucci, and M. Veldhorst, *Nature* **577**, 487 (2020), ISSN 1476-4687, URL <https://www.nature.com/articles/s41586-019-1919-3>.

[2] N. W. Hendrickx, W. I. L. Lawrie, M. Russ, F. van Riggelen, S. L. de Snoo, R. N. Schouten, A. Sammak, G. Scappucci, and M. Veldhorst, *Nature* **591**, 580 (2021), ISSN 1476-4687, URL <https://www.nature.com/articles/s41586-021-03332-6>.

[3] D. Jirovec, A. Hofmann, A. Ballabio, P. M. Mutter, G. Tavani, M. Botifoll, A. Crippa, J. Kukucka, O. Sagi, F. Martins, et al., *Nature Materials* **20**, 1106 (2021), URL <https://www.nature.com/articles/s41563-021-01022-2>.

[4] K. Aggarwal, A. Hofmann, D. Jirovec, I. Prieto, A. Sammak, M. Botifoll, S. Martí-Sánchez, M. Veldhorst, J. Arbiol, G. Scappucci, et al., *Physical Review Research* **3**, L022005 (2021), URL <https://journals.aps.org/prresearch/abstract/10.1103/PhysRevResearch.3.L022005>.

[5] F. Vignneau, R. Mizokuchi, D. C. Zanuz, X. Huang, S. Tan, R. Maurand, S. Frolov, A. Sammak, G. Scappucci, F. Lefloch, et al., *Nano Letters* **19**, 1023 (2019), ISSN 1530-6984, URL <https://doi.org/10.1021/acs.nanolett.8b04275>.

[6] N. W. Hendrickx, M. L. V. Tagliaferri, M. Kouwenhoven, R. Li, D. P. Franke, A. Sammak, A. Brinkman, G. Scappucci, and M. Veldhorst, *Physical Review B* **99**, 075435 (2019), URL <https://link.aps.org/doi/10.1103/PhysRevB.99.075435>.

[7] F. De Palma, F. Oppliger, W. Jang, S. Bosco, M. Janík, S. Calcaterra, G. Katsaros, G. Isella, D. Loss, and P. Scarlino, *Nature Communications* **15**, 10177 (2024), ISSN 2041-1723, URL <https://www.nature.com/articles/s41467-024-54520-7>.

[8] M. Janík, K. Roux, C. Borja-Espinosa, O. Sagi, A. Baghdadi, T. Adletzberger, S. Calcaterra, M. Botifoll, A. Garzón Manjón, J. Arbiol, et al., *Nature Communications* **16**, 2103 (2025), ISSN 2041-1723, URL <https://www.nature.com/articles/s41467-025-57252-4>.

[9] O. Sagi, A. Crippa, M. Valentini, M. Janik, L. Baghumyan, G. Fabris, L. Kapoor, F. Hassani, J. Fink, S. Calcaterra, et al., *Nature Communications* **15**, 6400 (2024), ISSN 2041-1723, URL <https://www.nature.com/articles/s41467-024-50763-6>.

[10] E. Kiyooka, C. Tangchingchai, L. Noirot, A. Leblanc, B. Brun, S. Zihlmann, R. Maurand, V. Schmitt, E. Dumur, J.-M. Hartmann, et al., *Nano Letters* **25**, 562 (2025), ISSN 1530-6984, URL <https://doi.org/10.1021/acs.nanolett.4c05539>.

[11] A. Nigro, E. Jutzi, F. Oppliger, F. De Palma, C. Olsen, A. Ruiz-Caridad, G. Gadea, P. Scarlino, I. Zardo, and A. Hofmann, *ACS Applied Electronic Materials* **6**, 5094 (2024), URL <https://doi.org/10.1021/acsaelm.4c00654>.

[12] X. Mi, J. V. Cady, D. M. Zajac, P. W. Deelman, and J. R. Petta, *Science* **355**, 156 (2017), URL <https://www.science.org/doi/10.1126/science.aal2469>.

[13] A. Stockklauser, P. Scarlino, J. V. Koski, S. Gasparinetti, C. K. Andersen, C. Reichl, W. Wegscheider, T. Ihn, K. Ensslin, and A. Wallraff, *Physical Review X* **7**, 011030 (2017), URL <https://link.aps.org/doi/10.1103/PhysRevX.7.011030>.

[14] J. Dijkema, X. Xue, P. Harvey-Collard, M. Rimbach-Russ, S. L. de Snoo, G. Zheng, A. Sammak, G. Scappucci, and L. M. K. Vandersypen, *Nature Physics* **21**, 168 (2025), ISSN 1745-2481, URL <https://www.nature.com/articles/s41567-024-02694-8>.

[15] E. Fitzgerald, Materials Science Reports **7**, 87 (1991), ISSN 09202307, URL <https://linkinghub.elsevier.com/retrieve/pii/0920230791900069>.

[16] A. Sammak, D. Sabbagh, N. W. Hendrickx, M. Lodari, B. Paquelet Wuetz, A. Tosato, L. Yeoh, M. Bollani, M. Virgilio, M. A. Schubert, et al., Advanced Functional Materials **29**, 1807613 (2019), ISSN 1616-3028, URL <https://onlinelibrary.wiley.com/doi/abs/10.1002/adfm.201807613>.

[17] L. E. A. Stehouwer, A. Tosato, D. Degli Esposti, D. Costa, M. Veldhorst, A. Sammak, and G. Scappucci, Applied Physics Letters **123**, 092101 (2023), ISSN 0003-6951, URL <https://doi.org/10.1063/5.0158262>.

[18] S. J. Weber, K. W. Murch, D. H. Slichter, R. Vijay, and I. Siddiqi, Applied Physics Letters **98**, 172510 (2011), ISSN 0003-6951, 1077-3118, URL <https://pubs.aip.org/apl/article/98/17/172510/908316/Single-crystal-silicon-capacitors-with-low>.

[19] S. Probst, F. B. Song, P. A. Bushev, A. V. Ustinov, and M. Weides, Review of Scientific Instruments **86**, 024706 (2015), ISSN 0034-6748, 1089-7623, URL <https://pubs.aip.org/rsi/article/86/2/024706/360955/Efficient-and-robust-analysis-of-complex>.

[20] D. Jirovec, P. M. Mutter, A. Hofmann, A. Crippa, M. Rychetsky, D. L. Craig, J. Kukucka, F. Martins, A. Ballabio, N. Ares, et al., Physical Review Letters **128**, 126803 (2022), URL <https://link.aps.org/doi/10.1103/PhysRevLett.128.126803>.

[21] M. Valentini, O. Sagi, L. Baghmyan, T. De Gijsel, J. Jung, S. Calcaterra, A. Ballabio, J. Aguilera Servin, K. Aggarwal, M. Janik, et al., Nature Communications **15**, 169 (2024), ISSN 2041-1723, URL <https://www.nature.com/articles/s41467-023-44114-0>.

[22] S. Gevorgian, L. Linner, and E. Kollberg, IEEE Transactions on Microwave Theory and Techniques **43**, 772 (1995), ISSN 1557-9670, URL <https://ieeexplore.ieee.org/document/375223>.

[23] J. P. Turneaure, J. Halbritter, and H. A. Schwettman, Journal of Superconductivity **4**, 341 (1991), ISSN 1572-9605, URL <https://doi.org/10.1007/BF00618215>.

[24] L. Grünhaupt, N. Maleeva, S. T. Skacel, M. Calvo, F. Levy-Bertrand, A. V. Ustinov, H. Rotzinger, A. Monfardini, G. Catelani, and I. M. Pop, Physical Review Letters **121**, 117001 (2018), ISSN 0031-9007, 1079-7114, URL <https://link.aps.org/doi/10.1103/PhysRevLett.121.117001>.

[25] M. S. Khalil, M. J. A. Stoutimore, F. C. Wellstood, and K. D. Osborn, Journal of Applied Physics **111**, 054510 (2012), ISSN 0021-8979, URL <https://doi.org/10.1063/1.3692073>.

[26] Z. Chen, A. Megrant, J. Kelly, R. Barends, J. Bochmann, Y. Chen, B. Chiaro, A. Dunsworth, E. Jeffrey, J. Y. Mutus, et al., Applied Physics Letters **104**, 052602 (2014), ISSN 0003-6951, 1077-3118, URL <https://pubs.aip.org/apl/article/104/5/052602/828862/Fabrication-and-characterization-of-aluminum>.

[27] E. V. Zikiy, A. I. Ivanov, N. S. Smirnov, D. O. Moskalev, V. I. Polozov, A. R. Matanin, E. I. Malevannaya, V. V. Echeistov, T. G. Konstantinova, and I. A. Rodionov, Scientific Reports **13**, 15536 (2023), ISSN 2045-2322, URL <https://www.nature.com/articles/s41598-023-42332-6>.

[28] C. P. Bean and J. D. Livingston, Physical Review Letters **12**, 14 (1964), URL <https://link.aps.org/doi/10.1103/PhysRevLett.12.14>.

[29] E. Zeldov, A. I. Larkin, V. B. Geshkenbein, M. Konczykowski, D. Majer, B. Khaykovich, V. M. Vinokur, and H. Shtrikman, Physical Review Letters **73**, 1428 (1994), URL <https://link.aps.org/doi/10.1103/PhysRevLett.73.1428>.

[30] L. Nulens, N. Lejeune, J. Caeyers, S. Marinković, I. Cools, H. Dausy, S. Basov, B. Raes, M. J. Van Bael, A. Geresdi, et al., Communications Physics **6**, 1 (2023), ISSN 2399-3650, URL <https://www.nature.com/articles/s42005-023-01386-8>.

[31] A. Hofmann, D. Jirovec, M. Borovkov, I. Prieto, A. Ballabio, J. Frigerio, D. Chrastina, G. Isella, and G. Katsaros, arXiv:19910.05841 (2019), URL <http://arxiv.org/abs/1910.05841>.

[32] W. C. Dunlap and R. L. Watters, Physical Review **92**, 1396 (1953), ISSN 0031-899X, URL <https://link.aps.org/doi/10.1103/PhysRev.92.1396>.